Journal of Power Sources 189 (2009) 240–247

Contents lists available at ScienceDirect

Journal of Power Sources

journal homepage: www.elsevier.com/locate/jpowsour

Preparation of the electrochemically formed spinel-lithium manganese oxides

Katsumi Katakura [a,*], Kohei Wada [a], Yoshiyuki Kajiki [a], Akiko Yamamoto [a], Zempachi Ogumi [b]

[a] Department of Chemical Engineering, Nara National College of Technology, 22 Yata-cho Yamotokoriyama, Nara 639-1080, Japan
[b] Graduate School of Engineering, Kyoto University, Nishikyo-ku, Kyoto 615-8510, Japan

ARTICLE INFO

Article history:
Received 31 July 2008
Received in revised form 9 September 2008
Accepted 15 September 2008
Available online 21 September 2008

Keywords:
Spinel-$LiMn_2O_4$
Electrochemical precipitation
Nanostructure
Lithium
Cathode

ABSTRACT

Electrochemically formed spinel-lithium manganese oxides were synthesized from manganese hydroxides prepared by a cathodic electrochemical precipitation from various concentrations of manganese nitrate solutions. Two types of manganese hydroxides were formed from diluted and concentrated $Mn(NO_3)_2$ aqueous solutions. Uniform and equi-sized disk shaped $Mn(OH)_2$ crystals of 0.2–5 μm in diameter were obtained on a Pt substrate after the electrochemical precipitation from lower concentration of ranging from 2 mmol dm^{-3} to 2 mol dm^{-3} $Mn(NO_3)_2$ aq., while the grass blade-like precipitate which is ascribed to manganese hydroxide with 20–80 μm long and 1–5 μm wide were formed from concentrated $Mn(NO_3)_2$ aq.

Both manganese hydroxides gave the electrochemically formed spinel-$LiMn_2O_4$ onto a Pt sheet, which is ready for electrochemical measurement, after calcination of the Li incorporated precipitate at 750 °C without any additives. While the shape and size of the secondary particle frameworks (aggregates) of the electrochemically formed spinel-$LiMn_2O_4$ can be controlled by the electrolysis conditions, the nanostructured primary crystals of 200 nm in diameter were obtained in all cases except that the fiber-like nanostructured spinel-$LiMn_2O_4$ crystals with 200 nm in diameter were obtained from concentrated $Mn(NO_3)_2$ aq. Though these two types of electrochemically formed spinel-$LiMn_2O_4$ showed well-shaped CVs even in higher scan rates, it would be suitable for high power density battery applications. These behaviors are assumed to be ascribed to the crystal size and shape of the processed spinel-$LiMn_2O_4$.

1. Introduction

Various kinds of lithium insertion compounds have been synthesized for use in rechargeable lithium batteries. Lithium nickel oxides, lithium cobalt oxides, and their derivatives, such as $LiCo_{1/3}Ni_{1/3}Mn_{1/3}O_4$, etc. are one of the traditional cathode materials for commercial lithium ion batteries. Among them, spinel-$LiMn_2O_4$ and derivatives, have been recognized to be one of the promising cathode materials used for 4 V rechargeable lithium ion batteries [1–7]. For electric and/or hybrid vehicles application, recently, much attention has been made to develop lithium ion batteries which exhibit not only high energy density but also high power density. For the fast charge–discharge application purpose, nanostructured cathode materials have been focused on [8–10].

Generally, synthesis of spinel-$LiMn_2O_4$ is divided into two categories. In the former case, spinel-$LiMn_2O_4$ particles are mixed with some additives such as, carbon black and PVDF, and the mixture is painted onto a current corrector to fabricate an actual electrode. Generally, spinel-$LiMn_2O_4$ is synthesized via calcination of manganese oxides and lithium hydroxide or salts mixtures [1–5,11,12]. Various kinds of lithium insertion compounds have been synthesized for use in rechargeable lithium batteries. Some researchers reported other methods such as, sol–gel and hydrothermal synthesis [13,14]. In the latter category, on the other hand, spinel-$LiMn_2O_4$ was prepared directly onto an electrode substrate using CVD or PVD, for example, in the laser ablation like process [6,7,15–17]. In these cases, the obtained spinel-$LiMn_2O_4$ electrode is usually used for fundamental studies on electrochemical behaviors of spinel-$LiMn_2O_4$ and is not used for commercial purposes because of its higher cost than the one prepared by the conventional method.

Previously, we reported the new preparation of the electrochemically formed spinel-lithium manganese oxide from the electrochemically precipitated manganese hydroxide which was deposited onto a Pt substrate by galvanostatic reduction of $Mn(NO_3)_2{\cdot}6H_2O$ solution [18]. The preparation scheme of the electrochemically formed spinel-lithium manganese oxide is shown in Fig. 1. The spinel-$LiMn_2O_4$ formed directly on a Pt substrate by calcination of the lithiated manganese hydroxides at 750 °C. This method achieved nanostructured spinel-$LiMn_2O_4$ crystals brought into direct contact with a Pt substrate without any additives and was already prepared for the electrochemical measurements, as is.

* Corresponding author. Tel.: +81 743 55 6160; fax: +81 743 55 6169.
E-mail address: katakura@chem.nara-k.ac.jp (K. Katakura).

0378-7753/$ – see front matter © 2008 Elsevier B.V. All rights reserved.
doi:10.1016/j.jpowsour.2008.09.042

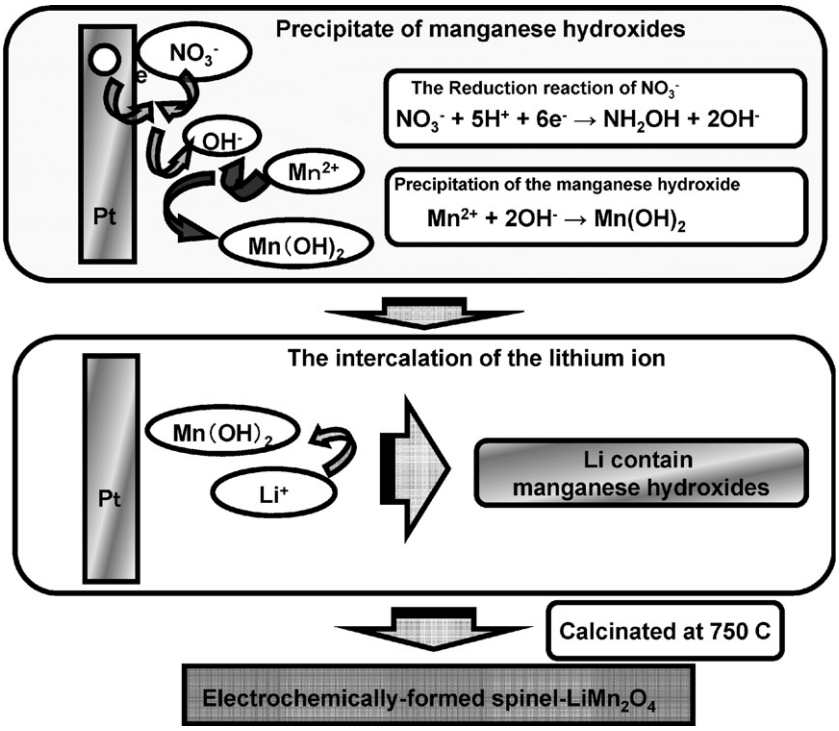

Fig. 1. The synthesis scheme of the electrochemically formed spinel-$LiMn_2O_4$.

The obtained spinel-$LiMn_2O_4$ showed high rate charge–discharge capability.

In this study, the new synthesis described above was adopted to obtain spinel-$LiMn_2O_4$ directly onto a substrate from wide concentration range of $Mn(NO_3)_2$ aqueous solutions. Manganese hydroxides were precipitated electrochemically from wide concentration range of $Mn(NO_3)_2$ aq. Although the cathodic electrochemical precipitation of nickel hydroxide on a substrate from a nickel nitrate aqueous solution is a well known technique for a nickel hydroxide cathode fabrication [19–22], in our knowledge, preparation of manganese hydroxide using this technique has been rarely reported [18]. For example, manganese hydroxide fabrication on a substrate is usually done by chemical precipitation technique [23].

The effect of $Mn(NO_3)_2$ concentration on the formation of manganese hydroxides and the morphology, the size and the electrochemical behavior of the electrochemically formed spinel-$LiMn_2O_4$ on a substrate from wide concentration range of $Mn(NO_3)_2$ aqueous solutions are discussed.

2. Experimental

The electrochemically formed $LiMn_2O_4$ was synthesized on a platinum sheet of 10 mm × 10 mm × 0.1 mm as described in our previous work. The outline of the process is as follows. The Pt sheet, a Pt counter electrode, and sat. Ag/AgCl reference electrodes were immersed in a manganese nitrate aqueous solution to configure a three-electrode electrochemical cell. The galvanostatic reduction of a manganese nitrate was conducted by applying a constant current between a working electrode and a counter electrode for a given time at 30 °C. When precipitate was formed on the Pt working electrode, the Pt was immersed in an air saturated 2 mol dm^{-3} LiOH aqueous solution for several hours, so that the lithium ion could be incorporated into the precipitate. The precipitates on the Pt sheet was rinsed several times with de ionized water and then calcined at 750 °C in the air for 24 h to obtain a electrochemically formed $LiMn_2O_4$ on the Pt sheet.

The electrochemical precipitation was also conducted using the electrochemical quartz crystal microbalance (EQCM). An EQCM (HOKUTO DENKO Model EQCMH101) was utilized to make in situ mass measurements of the deposits on a planar gold EQCM electrode during galvanostatic reduction of the manganese nitrate solution. A cell configuration for the EQCM measurements is illustrated in Fig. 2. Fig. 2 also shows the EQCM probe consists of a quartz crystal sputtered with a gold thin layer. The geometric area of a gold electrode attached to the quartz crystal was 0.204 cm^2 and the resonant frequency of the reference quartz crystal was 10 MHz. The frequency of the EQCM probe was measured with a PC equipped frequency counter card (Saunders and Associates, Inc. High Frequency Counter Card) to evaluate the mass of the deposit during the electrochemical precipitation reaction. The mass of the deposit was calculated from the frequency difference between the precipitates deposited EQCM electrode and the bare one using the Sauerbrey Eq. (1). The frequency change of 1 Hz corresponds to the mass change of 1.1 ng.

$$\Delta f = \frac{-2f_0^2 \Delta m}{A\left(\mu_q \rho_q\right)^{1/2}} \quad (1)$$

where Δf is the frequency difference, f_0 is the resonant frequency, Δm is the increase in mass of deposits, A is the electrode surface area, μ and ρ are the shear modulus and the density of quartz crystal, respectively.

Characterization of the precipitates, the precursor, and the final product formed on the substrate were carried out using XRD (Shimadzu XDD1W Cu Kα, 40 kV, 30 mA) and SEM (JEOL JSM-5900LV) techniques. The total amount of manganese in the precipitates and the products were determined by induced coupled plasma

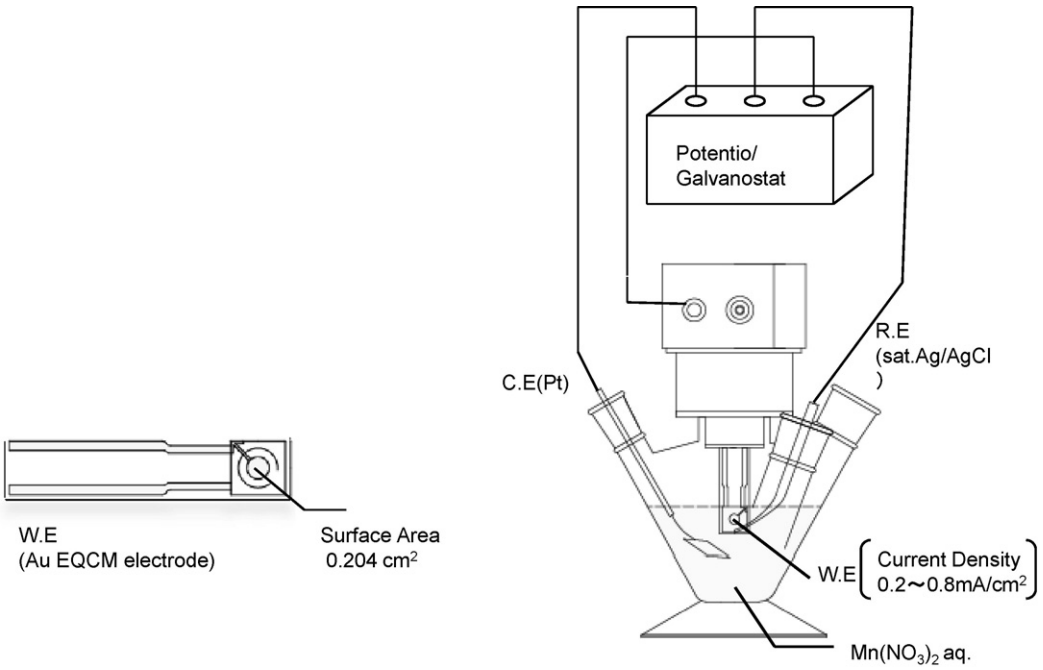

Fig. 2. The electrochemical cell for the cathodic precipitation of a manganese hydroxide.

spectroscopy (ICP) using a Shimadzu Model ICP-7000 ver. II spectrometer.

The electrochemical behavior of the product was examined using a three-electrode configuration cell in a 1.0 mold m^{-3} $LiClO_4$ aqueous solution with a sat. Ag/AgCl reference electrode. Since the product adhered tightly on the Pt substrate without any particular additives, such as PVDF and acetylene black, the electrochemical measurements of the products were carried out without further modification. The electrochemical measurement and galvanostatic electrolysis were carried out using a potentio/galvanostat model HSV-100 (HOKUTO DENKO) at room temperature.

All regents used in the experiment are regent grade without further purification.

3. Results and discussions

3.1. Cathodic electrochemical precipitation of manganese hydroxide

In Fig. 3, the mass of the manganese in the precipitates on a Pt sheet of 1 cm^2 after 10 min galvanostatic reduction at the current density of 0.4 mA cm^{-2} are plotted against the common logarithm of the manganese nitrate concentration of the electrolyte solution. The mass of manganese in the precipitates was determined by ICP measurement. As shown in Fig. 3, the concentration dependences of the mass of Mn are classified into four regions. When the manganese nitrate concentration was lower than 2 mmol dm^{-3}, the mass of manganese in the precipitate was low (Region A). The mass of manganese in the deposits of ca. 0.13 mg were obtained in the concentration range from 3 mmol dm^{-3} to 0.3 mol dm^{-3} (Region B). The mass lineally decreased with increasing the logarithm of the manganese nitrate concentration from 0.3 mol dm^{-3} to 3 mol dm^{-3} at which no precipitates formed on the substrate (Region C). As we reported previously, when the manganese nitrate concentration becomes higher than 3 mol dm^{-3}, more than 0.1 mg of manganese was found in the precipitate (Region D). A similar trend was observed when the mass of the precipitates obtained by EQCM measurement were plotted against the $Mn(NO_3)_2$ concentration. The XRD patterns of the precipitates shown in Fig. 4 indicated that manganese hydroxides crystal (JCPDF No. 18-0787) was formed in Regions B and C, and amorphous manganese hydroxides were formed in Region D. The mass of precipitates obtained by EQCM measurement was ca. 35% heavier than the mass of manganese hydroxides that calculated from the manganese contents in the precipitates by ICP measurement. The weight change of EQCM probes were monitored during galvanostatic reduction of $Mn(NO_3)_2$ aqueous solutions. From this weight difference, it is estimated that ca. 2.7 water molecules are involved in one $Mn(OH)_2$ molecular unit.

Streinz et al. reported the effect of current density and $Ni(NO_3)_2$ concentration on the rate of the electrochemical precipitation of $Ni(OH)_2$ precisely [22]. They concluded that (i) the deposition rate of $Ni(OH)_2$ is low in diluted $Ni(NO_3)_2$ solution at high current density (e.g. 0.01 mol dm^{-3} at 0.5 mA) due to the consump-

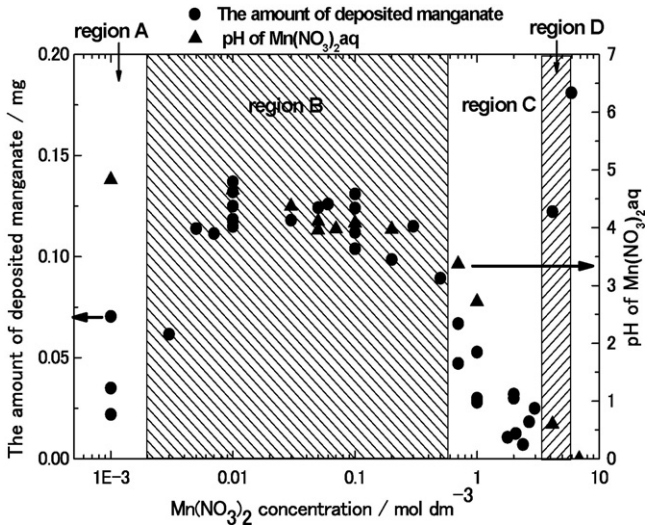

Fig. 3. The effect of $Mn(NO_3)_2$ concentration on the mass of Mn involved in the electrochemically precipitated $Mn(OH)_2$.

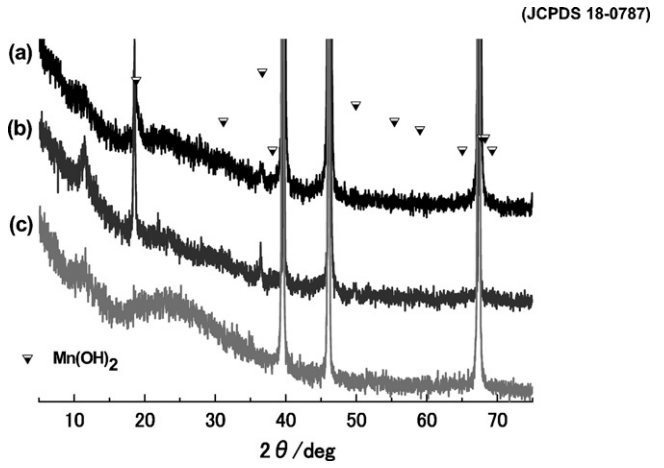

Fig. 4. X-ray diffraction patterns of the deposits precipitated from (a) 0.01 mol dm^{-3} $Mn(NO_3)_2$ [Region B], (b) 0. 1 mol dm^{-3} $Mn(NO_3)_2$ [Region B], and (c) 6 mol dm^{-3} $Mn(NO_3)_2$ [Region D].

tion of Ni^{2+} near the electrode surface, (ii) formation of soluble $Ni_4(OH)_4^{4+}$ decreases the deposition rate of $Ni(OH)_2$ at the higher $Ni(NO_3)_2$ concentration region and the decreased pH in concentrated $Ni(NO_3)_2$ solution is not the primary cause of the low deposition rate of $Ni(OH)_2$. Fig. 5 shows the dependence of the electric charge passed on the mass of the deposited $Mn(OH)_2$. As shown in Fig. 5, the mass of the deposit linearly increased with increasing the electric charge passed in Region B, while the immediate drop of deposition rate was observed in Region A. These results imply that their hypothesis can be applied to the rule of electrochemical precipitation of $Mn(OH)_2$ in Regions A and B. In Region C, the plot of the pH of $Mn(NO_3)_2$ aqueous solution versus logarithmic $Mn(NO_3)_2$ concentration and that of the mass of the deposits versus logarithmic $Mn(NO_3)_2$ concentration showed similar trend. The effects of solution pH on the solubility of $Mn(OH)_2$ was also examined by the precipitation titrations of various concentrations of $Mn(NO_3)_2$ aq. with 1.0 mol dm^{-3} LiOH. As shown in Fig. 6, the plots of the solution pH at the titration end-point obtained experimentally and those calculated theoretically from the solubility product of $Mn(OH)_2$ ($K_{sp} = 1.7 \times 10^{-13}$) against the $Mn(NO_3)_2$ concentration showed similar trend in Region C when the $Mn(NO_3)_2$ concentration was converted to the pH of the $Mn(NO_3)_2$ aq. In Region D, precipitation of $Mn(OH)_2$ was observed even though the solution pH was lower than that in 3 mol dm^{-3} of $Mn(NO_3)_2$, the upper concentration limit of Region C, where no precipitates were observed.

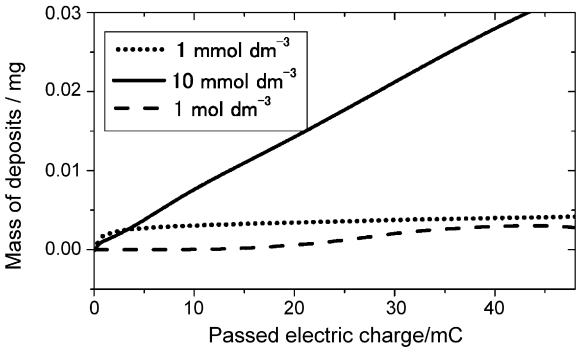

Fig. 5. The dependence of passed electric charge on the weight of the deposits prepared from different concentrations of $Mn(NO_3)_2$ aq.

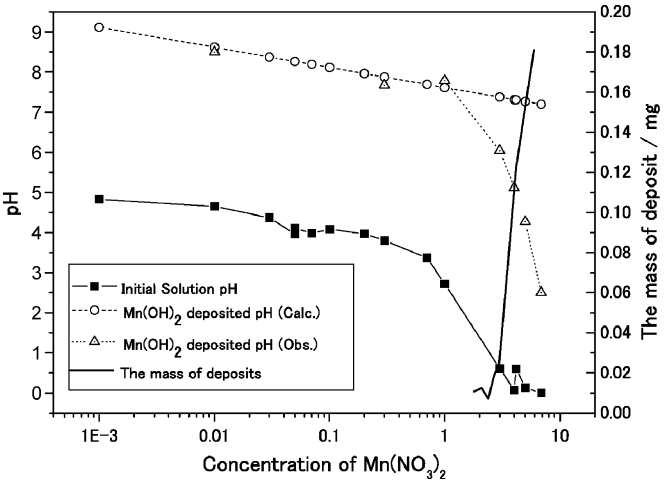

Fig. 6. The dependence of the normal logarithm of $Mn(NO_3)_2$ concentrations on the solution pHs at which $Mn(OH)_2$ precipitated. (Dotted line: experimental and broken line: theoretically calculated from the $Mn(OH)_2$ solubility product of $K_{sp} = 1.7 \times 10^{-13}$).

3.2. Shape and size of the precipitates

The SEM images of the precipitates prepared at different current density and $Mn(NO_3)_2$ concentration are shown in Fig. 7. The crystal diameter distributions at each electrolysis conditions are summarized in Fig. 8. As shown in Figs. 7 and 8, when the current density and the $Mn(NO_3)_2$ concentration were kept at constant values, uniform and equi-sized crystals are formed on the substrate after electrochemical precipitation. At the lower $Mn(NO_3)_2$ concentration regions, where $Mn(OH)_2$ crystals are formed, disk shaped crystals with different diameter and thickness were formed on the substrate. The diameter and thickness of the crystals tend to decrease with increasing the current density and decreasing the $Mn(NO_3)_2$ concentration, and vice versa. In contrast to the disk shaped crystals formed in the lower concentration region (Regions B and C) the grass blade-like precipitates of 20–80 μm long and 1–5 μm wide which is assumed to be an amorphous $Mn(OH)_2$ were formed in Region D (the concentrated $Mn(NO_3)_2$) as we reported previously [18]. The diameter and thickness of the precipitates deposited from different electrolysis conditions are summarized in Table 1. The current densities and the concentration of $Mn(NO_3)_2$ influenced the size of the crystals. If current density become high and the concentration of Mn^{2+} become low, a nucleation of the $Mn(OH)_2$ becomes a dominant reaction and the small size crystals are obtained. In opposite case, growth of $Mn(OH)_2$ crystal becomes a dominant process and the large crystals are grown. These phenomena are similar to those found in metal deposition process

Table 1
The size of the electrochemically precipitated.

$Mn(NO_3)_2$ (mol dm^{-3})	Current density (mA cm^{-2})	Diameter, d (μm)
6	0.4	40 (length)
0.6	0.2	5.5
	0.4	3.75
	1.6	5.5
	3.2	3.25
0.1	0.4	2.8
0.01	0.4	1.1
0.002	0.2	1.3
	0.4	1.0
	0.8	1.4
	1.6	0.65
	3.2	0.25

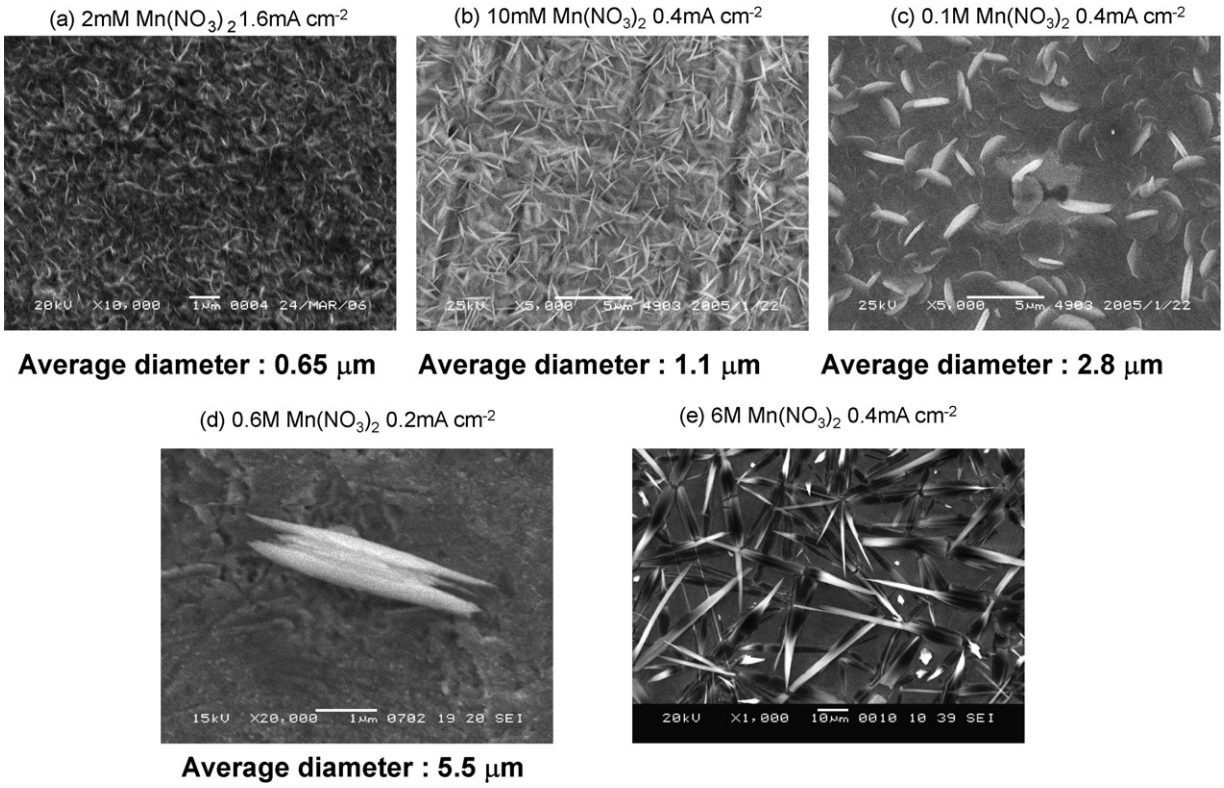

Fig. 7. SEM images of the deposits precipitated from (a) 2 mmol dm^{-3} $Mn(NO_3)_2$ at 1.6 mA cm^{-2}, (b) 10 mmol dm^{-3} $Mn(NO_3)_2$ at 0.4 mA cm^{-2}, (c) 0.1 mol dm^{-3} $Mn(NO_3)_2$ at 0.4 mA cm^{-2}, (d) 0.6 mol dm^{-3} $Mn(NO_3)_2$ at 0.2 mA cm^{-2}, and (e) 6 mol dm^{-3} $Mn(NO_3)_2$ at 0.4 mA cm^{-2}.

[25]. Therefore crystal size of the $Mn(OH)_2$ can be controlled by the electrolysis conditions, in Regions B and C.

It is assumed that the solubility of $Mn(OH)_2$ increases with decreasing the solution pH. In Fig. 6, however, when the concentration of $Mn(NO_3)_2$ was high, $Mn(OH)_2$ precipitation occurred even though the solution pH was low. Morphological difference among the two types of $Mn(OH)_2$ precipitated from low and concentrated $Mn(NO_3)_2$ are ascribed to a change in the formation process of $Mn(OH)_2$. Fig. 8 shows the overview of the concentration and current density dependence of the $Mn(OH)_2$ crystal size distribution. At lower current density region, the size of the crystals is identical and uniform in diameter.

As mentioned previously, $Mn(OH)_2$ can precipitate even though the solution pH was low in Region D. At the present, however, the structure of $Mn(OH)_2$ formed from concentrated $Mn(NO_3)_2$, such as $Mn(NO_3)_2{\cdot}6H_2O$ solution has not been clarified. The reason why the solubility become low in such low solution pH and the structure of the $Mn(OH)_2$ are needed to be clarified.

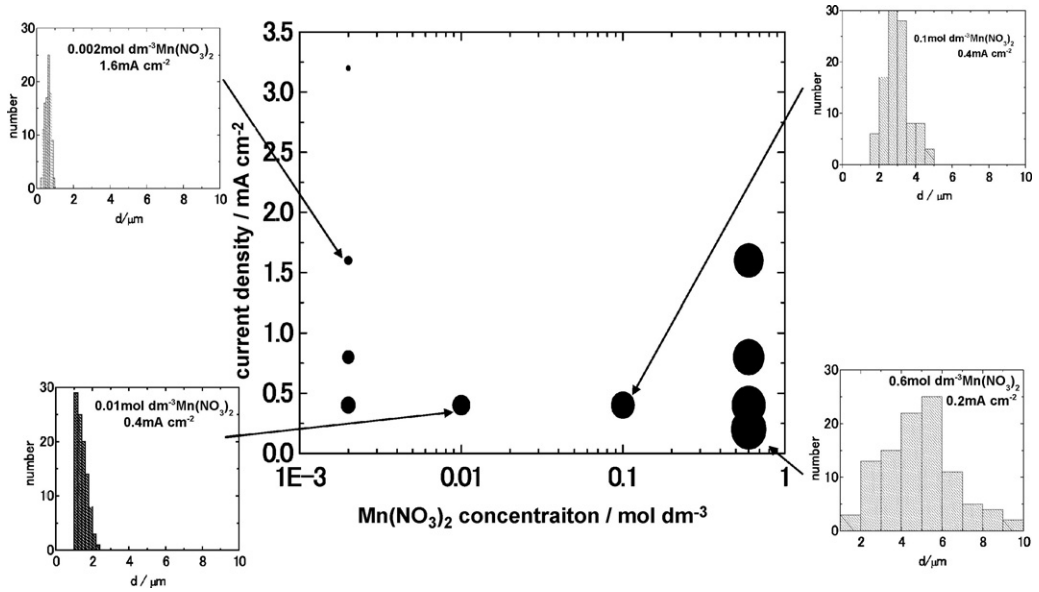

Fig. 8. The concentration and current density dependence of the crystal size distribution.

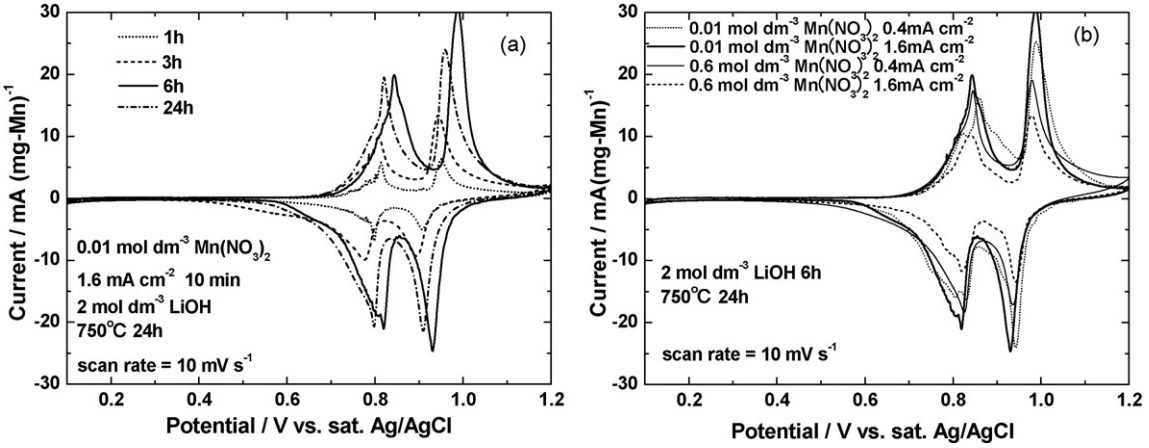

Fig. 9. Cyclic voltammograms of the $LiMn_2O_4$/Pt electrode at different immersion time measured in 1 mol dm^{-3} $LiClO_4$. (a) The effect of 2 mol dm^{-3} LiOH Immersion time and (b) the effect of electrolysis conditions.

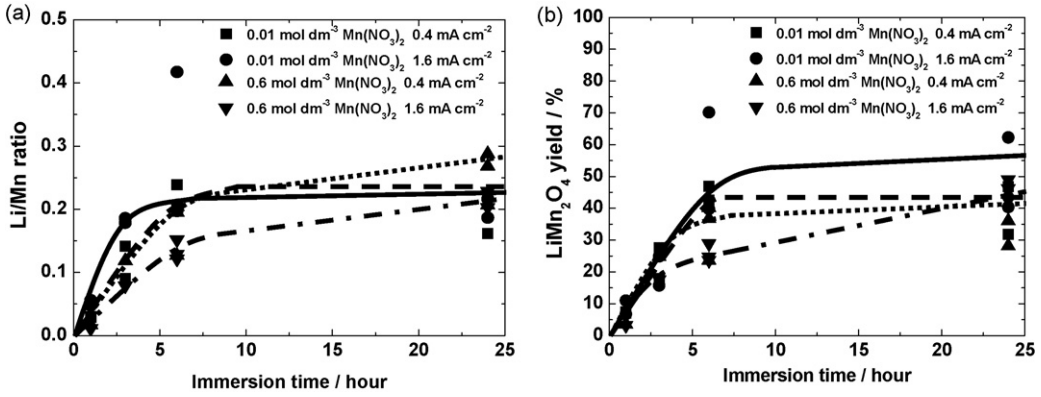

Fig. 10. SEM images of the electrochemically precipitated $Mn(OH)_2$ after soaking in 2 mol dm^{-3} LiOH (left images) and those of electrochemically prepared $LiMn_2O_4$ prepared after calcination at 750 °C for 24 h (right images).

3.3. *Electrochemistry and morphology of an electrochemically formed spinel-$LiMn_2O_4$*

In order to obtain electrochemically formed spinel-$LiMn_2O_4$, the $Mn(OH)_2$ precipitated from various $Mn(NO_3)_2$ concentrations and current densities were immersed in 2 mol dm^{-3} LiOH for several hours followed by calcined them at 750 °C for 24 h in the air. Martin et al. prepared nanostructred-spinel-$LiMn_2O_4$ tubules on a substrate directly without any additives by template method [24]. They used aqueous system to examine an electrochemical property of the sample. In order to use their nanostructred-spinel-$LiMn_2O_4$ tubules and our previous reported electrochemically formed spinel-$LiMn_2O_4$ as references, the electrochemical measurements of the final products were carried out in a 1.0 mol dm^{-3} $LiClO_4$ aqueous solution. As shown in Fig. 9, the cyclic voltammogram (CV) of the final product also indicated that the product should be ascribed to be a spinel-$LiMn_2O_4$ and the peak current of the CV increased with increasing the immersion time of the precipitate in a LiOH aqueous solution (as mentioned below). The charge–discharge behaviors of the electrodes obtained in Region B showed well-shaped cyclic voltammograms in 1.0 mol dm^{-3} $LiClO_4$ aqueous solution (Fig. 9(a)) at fairly high scan rate. As shown in Fig. 9(b), the electrolysis conditions did not affect the peak separations of the two redox current peaks. It seemed that the peak separations was not influenced by secondary particle size but was influenced by the primary crystal size of the spinel-$LiMn_2O_4$. In the present electrolysis conditions, the size of the primary crystal size was almost identical. In contrast to the rate capability of the electrochemically formed spinel-$LiMn_2O_4$, the Li^+ incorporation rate to the $Mn(OH)_2$ tend to increase with decreasing the crystal thickness.

The XRD pattern of the final product shown on curves in Fig. 10 is in good agreement with that of the spinel-$LiMn_2O_4$ and the product contains both spinel-$LiMn_2O_4$ and Mn_2O_3. Both the XRD pattern and the cyclic voltammograms of the calcined product indicated

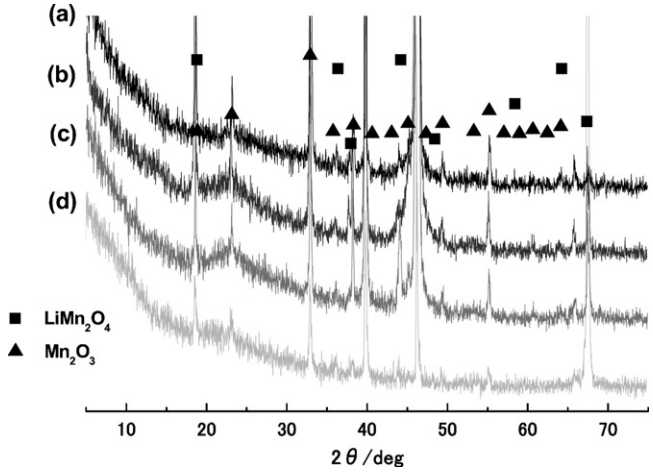

Fig. 11. Immersion time dependence of (a) Li/Mn ratios and (b) $LiMn_2O_4$ yields.

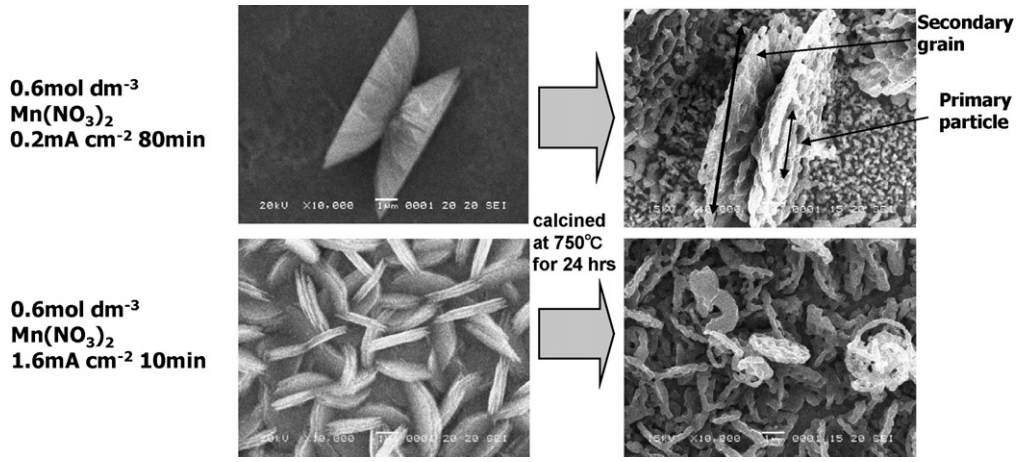

Fig. 12. X-ray diffraction patterns of the precipitates prepared from 0.6 mol dm^{-3} $Mn(NO_3)_2$ with various current densities which soaked in 2 mol dm^{-3} LiOH followed by calcined at 750 °C. (a) 3.2 mA cm^{-2}, (b) 1.6 mA cm^{-2}, (c) 0.4 mA cm^{-2}, and (d) 0.2 mA cm^{-2}.

that a electrochemically formed spinel-$LiMn_2O_4$ were obtained on the Pt sheet not only in Region D but also the lower $Mn(NO_3)_2$ concentration region, such as Region B.

As shown in Fig. 11, the SEM images of the product before and after calination indicated that the appearance of the calcined crystals are almost identical to those of precursors and they depended on the applied current density and $Mn(NO_3)_2$ concentration. In all cases, nanostructure crystals of 200 nm in diameter and 1 μm in length are formed in the secondary particle framework whose size and appearance are almost identical to those of their precursors. In other words, the size of the secondary particle can be controlled by applied current density, $Mn(NO_3)_2$ concentration, and other electrolysis conditions.

The results indicate that spinel-$LiMn_2O_4$ electrode obtained from the new method shows good charge–discharge performance not only in Region D but also in Region B.

The contents of the spinel-$LiMn_2O_4$ in the final products, those are assumed to be a yield of the electrochemically formed spinel-$LiMn_2O_4$, were evaluated from dividing the capacities of the final products by the theoretical capacities of the products, which were estimated from the amount of the total manganese deposited on the substrate based on the theoretical capacity of a spinel-$LiMn_2O_4$. The yields are plotted against the immersion time of the precipitate in Fig. 12. Here, the yield increased with increasing the immersion time of the precipitates up to ca. 10 h. When the electrochemically precipitated manganese hydroxide formed from 10 mmol dm^{-3} $Mn(NO_3)_2$, was immersed in a 3 mol dm^{-3} LiOH aqueous solution for 24 h the yields of ca. 60% was achieved.

The electrode showed well-shaped charge–discharge behaviors in an aqueous solution even though the scan rate was 10 times higher than that taken in a non-aqueous electrolyte system. The peak separations of the redox peaks for the electrochemically formed spinel-$LiMn_2O_4$ are almost identical to those for the spinel-$LiMn_2O_4$ tubules having 230 nm in diameter. These results indicated that spinel-$LiMn_2O_4$ electrode obtained from the new method showed good charge–discharge performance in an aqueous system. In the present work, therefore, the electrochemically formed spinel-$LiMn_2O_4$ performance was evaluated in an aqueous system.

The preliminary experiments indicated that the electrochemical behaviors of an electrochemically formed spinel-$LiMn_2O_4$ prepared in this study were similar to those reported for a thin film $LiMn_2O_4$ having 200 nm thick [17], even though the electrical contact of spinel-$LiMn_2O_4$ crystals and a substrate seemed smaller than the thin film case. Fiber-like nanostructured crystals obtained from the present procedure thought to be one of the reasons of the higher rate capability. The electrochemically formed spinel-$LiMn_2O_4$ could be suitable to enhance the rate capability of the spinel-$LiMn_2O_4$ electrode.

4. Conclusion

We succeeded the cathodic electrochemical precipitation of the both crystalline and amorphous like manganese hydroxides on the substrate. Two types of manganese hydroxides were formed from diluted and concentrated $Mn(NO_3)_2$ aqueous solutions. Uniform and equi-sized $Mn(OH)_2$ crystals of 0.2–5 μm in diameter were obtained on a Pt substrate after the electrochemical precipitation in lower $Mn(NO_3)_2$ concentration of ranging from 2 mmol dm^{-3} to 3 mol dm^{-3}, while the grass blade-like precipitate which is ascribed to manganese hydroxide with 20–80 μm long and 1–5 μm wide were formed from concentrated $Mn(NO_3)_2$ aq.

Two types of the manganese hydroxides were used as precursors of electrochemically formed spinel-lithium manganese oxides. The electrochemically formed spinel-$LiMn_2O_4$ was formed on a Pt sheet after calcination of the Li incorporated precursors at 750 °C without any additives. When the electrochemically precipitated manganese hydroxide was kept in an LiOH aqueous solution, Li^+ was incorporated in it.

While the shape and size of the secondary particle frameworks (aggregates) of the electrochemically formed spinel-$LiMn_2O_4$ can be controlled by the electrolysis conditions, the nanostructured primary crystals of 200 nm in diameter were obtained in all cases except that the fiber-like nanostructured spinel-$LiMn_2O_4$ crystals with 200 nm in diameter were obtained from concentrated $Mn(NO_3)_2$ aq. These two types of electrochemically formed spinel-$LiMn_2O_4$ showed well-shaped CVs even in higher scan rates. These behaviors are assumed to be ascribed to the crystal size and shape of the processed spinel-$LiMn_2O_4$.

The aggregate of the fiber-like nanostructured spinel-$LiMn_2O_4$ crystals with 200 nm in diameter was obtained on a substrate without any additives by calcination of the Li incorporated precipitate at 750 °C. The processed electrochemically formed spinel-$LiMn_2O_4$ was tightly attached to the substrate and was already for electrochemical measurement as is. The electrochemically formed spinel-$LiMn_2O_4$ showed well-defined CVs even in faster scan speeds. The fast charge discharge properties of the electrochemically formed spinel-$LiMn_2O_4$ are assumed to be ascribed to the

primary crystal size and shape. The secondary particle size does not play the important rule to the charge–discharge rate capability.

This process could be applied not only to preparation of substituted spinel but also that of layered oxides. Further investigations are in progress and to be reported in the feature.

Acknowledgement

This study was supported by Grant-in-Aid for Scientific Research (C:No. 18510111), The Ministry of Education, Culture, Sports, Science and Technology of Japan.

References

[1] J.M. Tarascon, D. Guyomard, Electrochim. Acta 38 (1993) 1221.
[2] R.J. Gummow, A.M. de Kock, M. Thackeray, Solid State Ionics 69 (1994) 59.
[3] D.J. Guyomard, M. Tarascon, Solid State Ionics 69 (1994) 222.
[4] Y. Xia, H. Takeshige, H. Noguchi, M. Yoshio, J. Power Sources 56 (1995) 61.
[5] Y. Guo, J.R. Dahn, J. Electrochem. Soc. 1443 (1996) 100.
[6] D. Singh, W.-S. Kim, V. Cracium, H. Hofmann, R.K. Singh, J. Electrochem. Soild-State Lett. 5 (2002) 198.
[7] P.L. Ji-Guang Zhang, J.A. Turner, C.E. Tracy, D.K. Benson, J. Electrochem. Soc. 146 (1999) 2001.
[8] S. Vivekanandhan, M. Venkateswarlu, N. Satyanarayana, J. Alloys Compds. 441 (2007) 284–290.
[9] J. Cabana, T. Valdés-Solís, M.R. Palacín, J. Oró-Solé, A. Fuertes, G. Marbán, A.B. Fuertes, J. Power Sources 166 (2007) 492–498.
[10] C.H. Jiang, S.X. Dou, H.K. Liu, M. Ichihara, H.S. Zhou, J. Power Sources 172 (2007) 410–415.
[11] R. Kanno, M. Yonemura, T. Kohigashi, Y. Kawamoto, M. Tabuchi, T. Kamiyama, J. Power Sources 97–98 (2001) 423.
[12] Y. Xia, M. Yoshio, J. Electrochem. Soc. 144 (1997) 4186.
[13] P. Barboux, J.M. Tarascon, F. Shokoohi, J. Solid State Chem. 94 (1991) 209.
[14] Y.M. Hon, K.Z. Fung, M.H. Hon, J. Eur. Ceram. Soc. 21 (2001) 515.
[15] M. Inaba, T. Doi, Y. Iriyama, T. Abe, Z. Ogimui, J. Power Sources 81-82 (1999) 554.
[16] K.A. Striebel, E. Sakai, E.J. Cairns, J. Electrochem. Soc. 149 (2002) 149.
[17] M. Mohamedi, D. Takahashi, T. Itoh, M. Umeda, I. Uchida, J. Electrochem. Soc. 149 (2002) A19.
[18] K. Katakura, S. Nishimura, Z. Ogumi, J. Power Sources 146 (2005) 217–221.
[19] W. Taucher, T.C. Adler, F.R. McLarnon, E.J. Cairns, J. Power Sources 81 (82) (1999) 554.
[20] T. Subbaiash, S.C. Mallick, K.G. Mishra, K. Sanjay, R.P. Das, J. Power Sources 112 (2002) 562.
[21] Murthy Mahesh, S.N. Gown, W.W. John, J.W. Van Ze, J. Electrochem. Soc. 143 (1996) 2319.
[22] C.C. Streinz, A.P. Hartman, S. Motupally, J.W. Weidner, J. Electrochem. Soc. 142 (1995) 1084.
[23] M.H. Ubeda, H. Herresa, H.T. Mishima, B.A.L. Mishima, H.M. Villullas, M.L. Teijelo, Elec. Acta 44 (1998) 513.
[24] N. Li, C.J. Patrissi, G. Che, C.R. Martin, J. Electrochem. Soc. 147 (2000) 2044.
[25] M. Paunovic, M. Schlesinger, Fundamentals of Electrochemical Deposition, 2nd Ed., John Wiley & Sons, Inc., New Jersey, 2006, Chapter 7.